MagPIE: A Dataset for Indoor Positioning with Magnetic Anomalies

David Hanley[1], Alexander B. Faustino[2], Scott D. Zelman[2], David A. Degenhardt[2], and Timothy Bretl[2]
Department of Electrical and Computer Engineering[1]
Department of Aerospace Engineering[2]
University of Illinois at Urbana-Champaign
Email: {hanley6,afausti2,szelman2,degenha2,tbretl}@illinois.edu

***Abstract*—In this paper, we present a publicly available dataset for the evaluation of indoor positioning algorithms that use magnetic anomalies. Our dataset contains IMU and magnetometer measurements along with ground truth position measurements that have centimeter-level accuracy. To produce this dataset, we collected over 13 hours of data (51 kilometers of total distance traveled) from three different buildings, with sensors both handheld and mounted on a wheeled robot, in environments with and without changes in the placement of objects that affect magnetometer measurements ("live loads"). We conclude the paper with a discussion of why these characteristics of our dataset are important when evaluating positioning algorithms.**

***Index Terms*—Magnetic Localization, Indoor Localization, Dataset, Comparison of Methods**

I. Introduction

Magnetic anomalies are variations in the Earth's magnetic field that can be used for indoor positioning of both smartphones and robots. In indoor environments, the absence of a global navigation satellite system necessitates alternative positioning methods. Some indoor localization strategies for smartphones (such as Qualcomm's Lumicast [1]) require infrastructure specifically for the purpose of positioning. In the case of Lumicast, a set of light fixtures must broadcast positioning signals using visible light communication (VLC). Wi-Fi based positioning, beyond requiring the presence of a number of access points, can also require knowing the position of these access points and can suffer inconsistent fingerprints due to blockage from users or other pedestrians [2]. In many cases, a localization solution that does not require such infrastructure is desired.

Several sensors used in robot or smartphone localization that do not require infrastructure like VLC lights or the use of access points include magnetometers, cameras, and LiDAR. Magnetometers offer several advantages to both camera and LiDAR localization. In robotic applications, there are some scenarios where cameras may not be allowed due to security and privacy concerns [3]. Performance of camera-based positioning can also be significantly degraded due to low lighting or smoke [4]. Magnetic field-based positioning systems, consisting of an inertial measurement unit (IMU) and magnetometer, have a cost advantage over other sensors commonly used for localization [5]. Table I compares the cost of a magnetometer that can be found on a robot or smartphone with an IMU, camera, or LiDAR system. Magnetometers, moreover, are ubiquitous on mobile robot platforms and smartphones.

TABLE I
Cost Comparison of Sensors used for Localization

Sensor	Example	Cost	Source
Smartphone IMU	InvenSense MPU-6500	$3.50	[6]
Magnetometer	NXP MAG3110	$1.46	[7]
Camera	mvBlueFOX-MLC200w	$310.00	[8]
LiDAR	Velodyne PUCK VLP-16	$7999.00	[9]

The use of magnetometers to localize a smartphone or robot indoors is becoming common. For example, companies such as IndoorAtlas have developed indoor positioning solutions using magnetic anomalies [10]. With respect to localization algorithms, methods exist to localize smartphones in a building using pedestrian dead reckoning (PDR) and a magnetic field [11]–[14]. There also exist methods for localizing smartphones using Wi-Fi and magnetic maps together [2], [15]–[18]. For example, when comparing methods for Wi-Fi surveying and localization with a magnetometer-based approach, Gao and Harle [16] found that magnetic signals were particularly useful for detecting loop closure with smartphones. Magnetometers have also been used to position cleaning robots, cars, and unmanned ground vehicles (UGVs) [4], [5], [19]–[21].

Considering the growing popularity of positioning with magnetic anomalies, it is necessary to establish publicly available datasets so that these methods can be compared. The first dataset presented for the purpose of evaluating positioning algorithms based on magnetic anomalies was the UJIIndoorLoc-Mag dataset of Torres-Sospedra et al [12]. This dataset collected magnetic field and IMU measurements from a smartphone in a 15×20 meter office space. Another dataset, presented by Barsocchi et al [22], was developed to compare approaches to positioning methods using inertial sensors and Wi-Fi to methods using inertial sensors and magnetometers.

Our primary contribution is to present a new, publicly available dataset—the Magnetic Positioning Indoor Estimation (MagPIE) dataset[1]—that can be used to further benchmark and study approaches to magnetic and inertial positioning. This

978-1-5090-7/17/$31.00 © 2017 IEEE

[1]http://bretl.csl.illinois.edu/magpie

dataset provides magnetometer, IMU, and ground truth position and orientation measurements collected in 723 separate trials over a total duration of more than 13 hours, a total distance of more than 51 kilometers, and a total area of more than 960 square meters. We describe the system, methods, and experiments used to produce this dataset in Sections II-IV.

The MagPIE dataset has three characteristics that differentiate it from what has been available previously:

- Data were collected from multiple buildings with a large total test area (960 square meters of floor space in three different buildings compared to, for example, 185 square meters in one building [22]). We show in Section V-A that methods of indoor positioning may perform quite differently in different buildings.
- Data were collected with sensors that were both handheld (as in prior datasets) and mounted on a wheeled robot (new to our dataset). We show in Section V-B that indoor positioning algorithms are, by necessity, different in these two cases, because of the presence or absence of well-defined steps into which IMU measurements can be segmented.
- Data were collected both with and without changes in the placement of objects that may affect magnetometer measurements. Prior datasets were based on the assumption that all magnetic anomalies are constant over time (i.e., are "dead magnetic loads"), while our dataset is based on the assumption that certain magnetic anomalies are only temporary (i.e., are "live magnetic loads"). We show evidence in Section V-C that supports this assumption.

Our dataset can provide a benchmark for testing magnetometer map surveying, localization, SLAM, and loop closure approaches. It can also be used to improve algorithms for PDR or gravitation tracking (such as Sarkka et al [23]).

II. Data Collection: System

A. Sensing Platforms

As our sensing platform, we used a Motorola Moto Z Play smartphone collecting magnetometer data at approximately 50 Hz and accelerometer and gyroscope data at approximately 200 Hz. The Allan standard deviation plots—which describe the angle and velocity random walk, bias instability, and rate random walk—of accelerometers and gyroscopes on the smartphone are shown in Figures 1 and 2. These plots were created from a 3908 second static test, and data used to produce them have been provided on the dataset website. The Allan standard deviation plots shown can be used to tune Kalman filtering approaches to positioning with this dataset (see El-Sheimy et al [24]). The norm of magnetometer measurements on the smartphone were found to have a standard deviation of 0.495 μT. The Motorola Moto Z Play was used for both pedestrian and UGV tests.

B. Ground Truth

The position and orientation estimates produced by an application using Google's Tango API on a Lenovo Phab 2 Pro were taken to be the ground truth measurements for our dataset. As a way to assess our ability to use Google's Tango as a source of ground truth for this application, we mapped and then localized our Phab 2 Pro inside a motion capture arena. We then computed the absolute trajectory error (ATE), as described by Sturm et al [25]. The root mean square absolute trajectory error over five different trials is shown in Table II. Figure 3 shows our two smartphones arranged for the UGV and walking case.

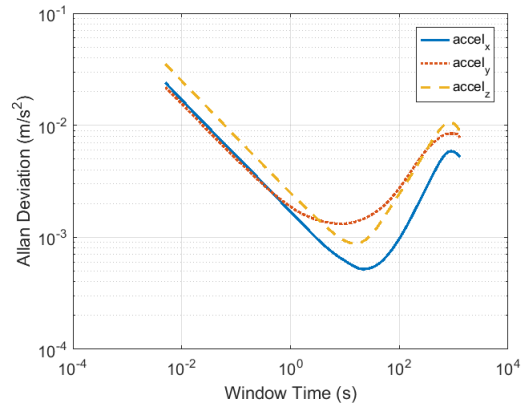

Fig. 1. Smartphone accelerometer Allan standard deviation, which describes the sensor's velocity random walk, bias instability, and rate random walk.

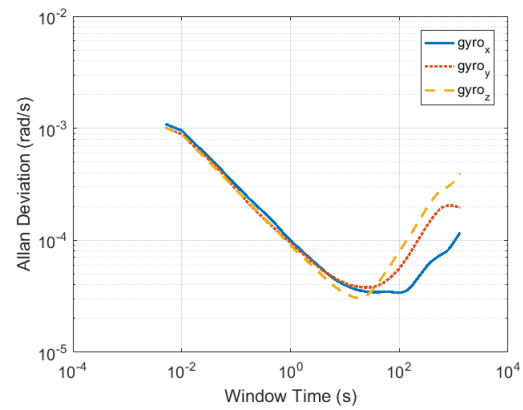

Fig. 2. Smartphone gyroscope Allan standard deviation, which describes the sensor's angle random walk, bias instability, and rate random walk.

III. Data Collection: Methods

Each trial of our dataset was collected according to the pipeline outlined in Figure 4. First, our test areas were mapped using the Google Tango application. Subsequently,

TABLE II
Root Mean Square ATE of Ground Truth Position Estimate

Trial	RMS ATE (cm)
1	2.92
2	3.13
3	4.20
4	4.19
5	3.52

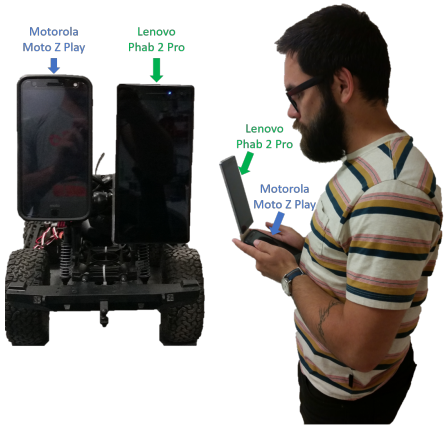

Fig. 3. The UGV platform with the Motorola Moto Z Play and Lenovo Phab 2 Pro (left) and our walking device (right).

we collected data on our smartphone and UGV outside to account for magnetometer biases. Immediately, prior to collecting all relevant magnetometer, accelerometer, gyroscope, and ground truth data, we kept our Motorola Moto Z Play still for approximately thirty seconds for coarse quasi-stationary initialization to be performed. While in between obtaining data for individual trials, we occasionally collected additional data for magnetometer calibration. Offline, we compared all magnetometer calibrations to ensure that significant biases were not inadvertently introduced during testing.

A. Mapping with Tango

We used Google Tango's API to create an application that can map an area and subsequently localize our Lenovo Phab 2 Pro in that map. In all cases, in order to ensure a higher quality map, we added visual features (in the form of fiducial markers called AprilTags [26]) to the test area prior to mapping. We explored each area and provided multiple opportunities for drift in the map to be corrected through the identification of loop closures. Each map of the environment was saved in an area description file. That file was then used to localize our test devices. Fiducial markers remained in the scene throughout this mapping process as well as during all subsequent tests.

B. Calibrating Magnetometers

Prior to our tests, we collected data to compute the hard iron offset vector, b_m, and soft iron matrix, Λ, of our magnetometers. These offsets were applied to raw magnetometer measurements as described by [27]:

$$m_c = \Lambda(m_{raw} - b_m). \tag{1}$$

A triad of uncalibrated and orthogonal magnetometers create an ellipsoid when spun about a point. The hard iron offset describes how far from the origin the center of that ellipsoid is, while the soft iron offset matrix describes the eccentricity of the ellipsoid. Equation 1 projects raw magnetometer measurements onto a sphere centered at the origin with a radius of approximately 53 μT, since this is roughly the magnitude of Earth's magnetic field in Urbana, IL.

C. Initialization

Prior to each test, we kept our test devices still for approximately thirty seconds to allow for the computation of the initial orientation of the device relative to the plumb-bob gravity vector, which we call quasi-stationary initialization. In particular, we computed coarse estimates of the initial orientation of the device by claiming that the direction cosine matrix (C) of the IMU's frame of reference in terms of the local frame of reference, which is NED, as described by Savage [28]:

$$C = \begin{bmatrix} C_{(1,1)} & C_{(1,2)} & C_{(1,3)} \\ 0 & \frac{C_{(3,3)}}{\sqrt{C_{(3,2)}^2 + C_{(3,3)}^2}} & \frac{-C_{(3,2)}}{\sqrt{C_{(3,2)}^2 + C_{(3,3)}^2}} \\ -\left(\frac{a_{SF}}{\|a_{SF}\|}\right)_x & -\left(\frac{a_{SF}}{\|a_{SF}\|}\right)_y & -\left(\frac{a_{SF}}{\|a_{SF}\|}\right)_z \end{bmatrix} \tag{2}$$

where

$$\begin{aligned} C_{(1,1)} &= C_{(2,2)}C_{(3,3)} - C_{(2,3)}C_{(3,2)} \\ C_{(1,2)} &= C_{(2,3)}C_{(3,1)} - C_{(2,1)}C_{(3,3)} \\ C_{(1,3)} &= C_{(2,1)}C_{(3,2)} - C_{(2,2)}C_{(3,1)}. \end{aligned}$$

Here $C_{(i,j)}$ refers to the element of C on the ith row and j^{th} column, a_{SF} is the specific force vector measured by our accelerometers (in m/s^2) and $(\cdot)_x$, $(\cdot)_y$, and $(\cdot)_z$ are the x, y, and z components of the contained vector respectively.

IV. Data Collection: Experiments

Leveraging the structure of previously used datasets (i.e. the UJIIndoorLoc-Mag dataset [12]), we separated our collection process into training and testing trials. Typically, we would anticipate that training trials are used to generate magnetic maps, while testing trials are used to assess how well proposed algorithms localize within these generated maps. To accommodate differing use cases, we performed tests for walking with a handheld phone (as if one was texting) and for a UGV. Finally, we conducted two different testing scenarios: one without any imposed changes to the magnetic field of the building (dead load cases) and a second set with objects (or live loads) added to the scene that change the magnetic field of the building.

A. The buildings and trial descriptions

We collected data in portions of three different buildings on the UIUC campus: the Coordinated Sciences Laboratory (CSL), Talbot Laboratory, and Loomis Laboratory. These buildings are depicted in Figure 5, and the portion of each building used in our dataset contain approximately 195, 295, and 470 square meters of area respectively. The number of training and testing trials for each building, platform, and test scenario are described in Table III. The table also reports the average density of magnetometer training measurements over the relevant area of the associated building in the dataset. Histograms of the time and distance traveled over all trials in the dataset are presented in Figure 6. In total, over 13 hours and 51 kilometers of data have been collected. On average, each test case was approximately 90 seconds and 101 meters long. The shortest test case by time was 21 seconds, and the shortest test case by distance traveled was 23 meters. In

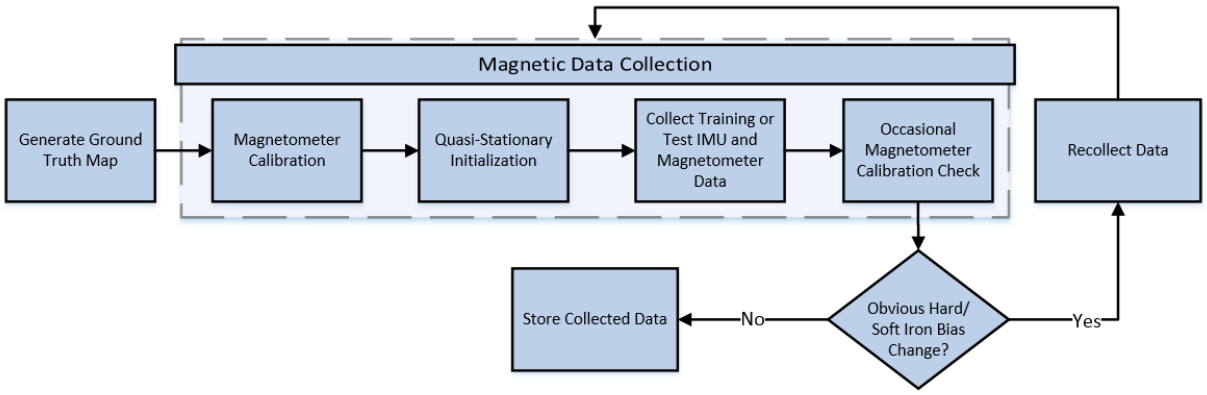

Fig. 4. The pipeline for collecting data for the MagPIE dataset. We first map each test area with our Lenovo Phab 2 Pro. Then the magnetometers are calibrated. The test device is subsequently held stationary, so that an initial estimate of the device's orientation can be computed. The data presented in the publicly available dataset is then collected. Throughout our tests, the magnetometer is calibrated again to ensure that biases were not inadvertently introduced.

(a) Coordinated Science Laboratory

(b) Talbot Laboratory

(c) Loomis Laboratory

Fig. 5. We collect data for mapping and localization in portions of three buildings: the first floor of the UIUC's Coordinated Sciences Laboratory, the third floor of Talbot Laboratory, and the first floor of Loomis Laboratory.

TABLE III
NUMBER OF TRAINING AND TESTING CASES AND DENSITY OF TRAINING CASES (IN MEASUREMENTS PER SQUARE METER)

Building and Platform	Num. Train Cases	Num. Dead Load Cases	Num. Live Load Cases	Mag. Density
CSL UGV	93	11	10	1615.1
CSL WLK	100	11	11	530.1
Talbot UGV	100	11	11	944.5
Talbot WLK	99	11	11	417.6
Loomis UGV	99	11	11	1907.2
Loomis WLK	100	12	11	4397.0

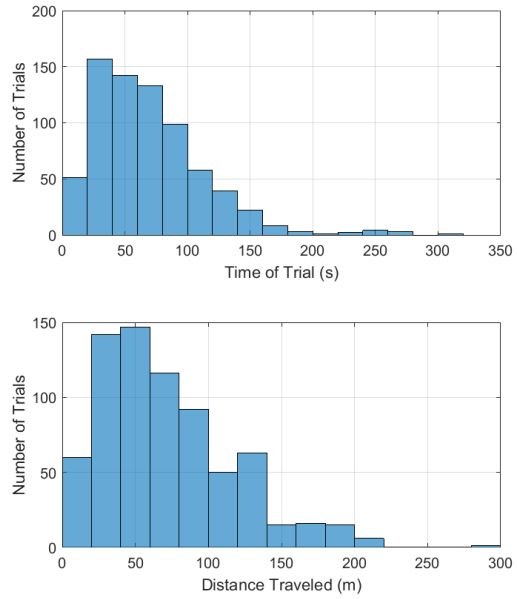

Fig. 6. Histograms of the distance traveled and time span of all trials.

addition, the longest test case by time was approximately 245 seconds, and the longest test case by distance was 297 meters.

B. File Descriptions

We structued our dataset such that each test or training trial contained five files: Initial_DCM#.txt, Output_accel#.txt, Output_gt#.txt, Output_gyro#.txt, Output_mag#.txt. The initial DCM files were the result of the coarse quasi-stationary initialization. The first column of the accelerometer, ground truth, gyroscope, and magnetometer files have been made to contain the time stamp of each measurement in seconds. The accelerometer, gyroscope, and magnetometer data have been made to list, in their subsequent columns, measurements along

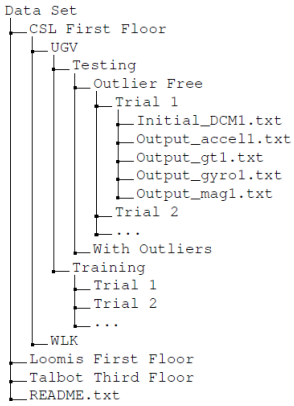

Fig. 7. Directory tree of the MagPIE dataset. Directories for walking trials are labeled WLK. Dead load test cases are labeled Outlier Free and live load test cases are labeled With Outliers.

the body-frame's x, y, and z axes (in that order and in m/s^2, rad/s, and μT respectively). The ground truth data has been made to list position and quaternion information respectively in subsequent columns. Our data was arranged in the file structure shown in Figure 7.

V. Discussion

Our dataset has three characteristics that differentiate it from what has been available previously: data were collected from multiple buildings with sensors that were both handheld and mounted on a wheeled robot both with and without changes in the placement of objects that affect magnetometer measurements. In this section, we discuss the ways in which indoor positioning algorithms depend on these three characteristics to motivate their inclusion in our dataset.

A. Differences Between Buildings

Previous datasets—such as the UJIIndoorLoc-Mag dataset or the dataset from Barsocchi et al [22]—only use data from one building in their dataset. Using the method presented by Li et al [2], we use training data and Gaussian process regression (GPR) to generate two sets of maps: Talbot UGV maps and Loomis UGV maps. Then, we compare the percent of the global maximum likelihood estimate (MLE) and local maximum a posteriori (MAP) estimate above a set of thresholds over all dead load test cases associated with each scenario. Finally, we compute the same estimates over all live load test cases for the Talbot UGV segment of the dataset. As a result, we see that there is a significant difference between two of our buildings, which motivates the inclusion of multiple buildings in our dataset.

1) Mapping with Gaussian Process Regression: We generate a map with GPR for each element of the magnetic field vector in the Google Tango frame of reference using our training magnetic field measurements and the ground truth locations and orientations of those measurements. We construct this map with the help of the GPML toolbox [29]. We take as our GPR kernel the squared exponential function and we also

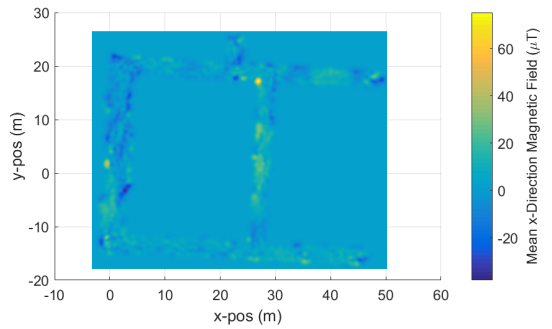

(a) x-Direction Field

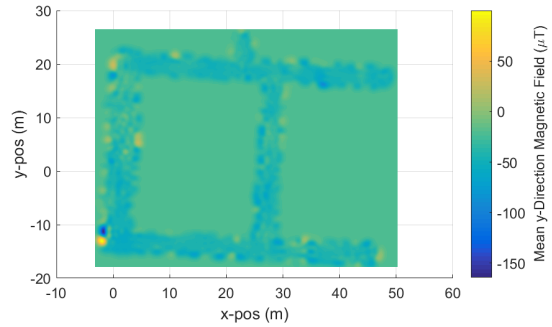

(b) y-Direction Field

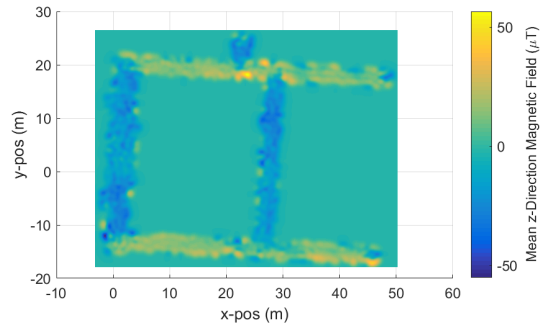

(c) z-Direction Field

Fig. 8. Map of expectation of the magnetic field vector computed using Loomis Laboratory UGV training data and Gaussian process regression.

assume a constant mean function. Our Loomis UGV dataset contains more than 444,000 data points for training our GPR algorithm, and our Talbot UGV dataset contains more than 475,000 data points for training. Due to memory limitations, we compute hyperparameters and a heat map using 75,000 randomly selected training points with 2,220 induced points and a variational free energy approximation [30]. The resulting GPR approximation computes a map of the expectation of the measurement from a calibrated magnetometer at any given point on the map as well as its variance. The map of the expectation of calibrated magnetometer measurements for the Loomis UGV case is shown in Figure 8. From the figure, the range of magnetic field measurements modeled by the map can be seen. Clearly, magnetic anomalies are present in the scene and can be quite large relative to Earth's magnetic field.

TABLE IV
PERCENT OF MEASUREMENTS AT OR ABOVE MAXIMUM LIKELIHOOD ESTIMATE OR MAXIMUM A POSTERIORI THRESHOLD

Threshold ($\times 10^{-5}$)	1.036	0.948	0.781	0.566	0.433
Loomis UGV Global MLE %	2.0	2.5	3.3	4.4	6.0
Talbot UGV Global MLE %	0.5	1.0	2.0	5.6	11.2
Talbot UGV Global MLE % (Live)	1.1	1.4	2.7	6.2	11.6
Loomis UGV Local MAP %	10.8	11.6	16.3	25.1	34.5
Talbot UGV Local MAP %	49.6	55.6	64.2	76.6	83.1
Talbot UGV Local MAP % (Live)	51.7	57.8	69.4	84.4	90.5

2) Localization: Using the framework from Li et al [2], we take as our state vector, θ, the two dimensional map position and an azimuth angle. Given calibrated magnetometer measurements, we search over a grid of states in the map to find the maximum likelihood estimate using Bayes' formula

$$p(\theta|m_c) = \frac{p(m_c|\theta)p(\theta)}{p(m_c)} \tag{3}$$

where the probability generated by the maps enable the computation of $p(m_c|\theta)$ using the multivariate Gaussian model

$$p(m_c|\theta) = \frac{\exp\left(-\frac{1}{2}\left[m_c - \mu_b(\theta)\right]^T Q^{-1}(\theta)\left[m_c - \mu_b(\theta)\right]\right)}{(2\pi)^{\frac{3}{2}}|Q(\theta)|^{\frac{1}{2}}} \tag{4}$$

where $\mu_b(\theta)$ are the mean values from the maps produced through Gaussian process regression and $Q(\theta)$ are the associated covariances from these maps. As with Li et al [2], $p(m_c)$ is a normalizing factor since it is not a function of the state. We compute a global MLE every half meter along all test trajectories. We then, following the same approach as Li et al [2], include a prior, $p(\theta)$, at the true state with a standard deviation of $3m$ to compute a local MAP estimate for all the test trajectories.

We compute, for the Loomis and Talbot UGV cases, the percent of tested points with a global MLE and local MAP estimate beyond a set of given thresholds in Table IV. While it is important to point out that such a map can be improved (with a resulting improvement in corresponding MLE and MAP estimation results), it is clear from the table that for our given mapping approach, there does exist a difference between the results associated with two of the buildings in our dataset. This result motivated collecting data from multiple buildings in the MagPIE dataset.

B. Differences Between Platforms

Indoor pedestrian positioning algorithms often use PDR [3], [11], [14]–[18]. Robots must use a numerically integrated inertial navigation system (INS) or an INS complemented by a dynamic model of the robot [31]. Rather than growing with time as an INS does, PDR error grows with the number of steps, which provides substantial advantages for a positioning algorithm operating with a pedestrian. PDR avoids time-related error growth by identifying steps taken and turns made by the pedestrian and associating a stride length with each step. From the perspective of a smartphone, steps produce a very noticeable pattern that enable PDR. Figure 9 shows a segment of the ground truth measurements (top) and accelerometer measurements (middle) in the z-direction from a small walking segment of our dataset. It is clear that steps result in sinusoidal motion on the smartphone in both the ground truth and in accelerometer measurements. For comparison, measurements from a UGV's accelerometers (bottom) do not have such a pattern. Due to the difference between pedestrian and UGV motion and the implications with respect to positioning algorithms, we choose to include both platforms in our dataset.

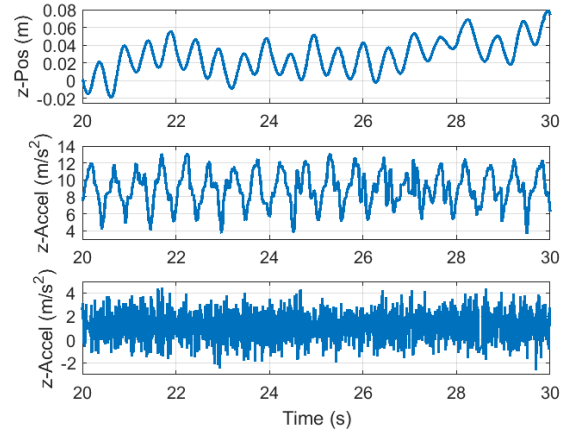

Fig. 9. Steps made by pedestrians cause a clear pattern that can be leveraged by PDR, which can be seen as a sinusoid in the z-direction of the ground truth measurements (top) and accelerometer measurements (middle) during a small portion of the MagPIE dataset. As a comparison, a segment of the z-direction of accelerometer measurements of a UGV trial is also included (bottom).

C. Differences Between Live Load and Dead Load Cases

In previous literature on localization and mapping based on magnetic anomalies, it has been assumed that the magnetic fields in buildings are constant over time. It is stated by Wang et al [3] that "anomalies are reasonably stable in a long period of time." In addition, Li et al [2] state that there exist "long temporal persistence in terms of direction and intensity" of a building's magnetic field. While Frassl et al [4] acknowledges that distortions in a building's magnetic field may occur due to moving objects like elevators or furniture, the field in a building still "appears to be stable over long periods of time." It is stated by Akai and Ozaki [21] that the "stability of the disturbed magnetic field over long periods of time has already been demonstrated." Finally, Robertson et al [32] also states that magnetic fields in buildings are "temporally stable."

Rather than assuming that the magnetic field in a building is static, we include test cases in our dataset wherein we move objects along the test trajectory that are meant to change the building's magnetic field. Thus, a positioning method may compare performance in the presence of larger innovations. Toward that end, we select eight potential candidate "live magnetic loads" that may alter the magnetic field in a building. We then place our UGV on rails and drive down a hallway twenty times: ten times without any object in the hallway

and then a second ten with a given object in the hallway. The results are shown in Figure 10. Based on this, we use a computer cart, an industrial fan, a table and chairs, and a toolbox to change the magnetic field in approximately half of our UGV test trials. Performing a similar routine for our walking case, we choose to include a table and chairs and a computer cart in approximately half of our walking test trials.

Relative to the size of the map or the number of points sampled along the test trajectories in our localization algorithm, the number of distortions produced by the live magnetic loads are few. Thus, because test trajectories between live load cases and dead load cases are not kept constant, it is not surprising that live loads do not dominate the results produced in Table IV. However, as shown in Figure 10, this segment of the dataset may be important for comparing positioning algorithms that look to reject such outliers. Thus, while we present evidence that these live magnetic loads cause differences in the magnetic field of a building, more work must be done to understand their impact on localization algorithms. Due to these results, and the need for further study, we include live loads in our dataset.

Acknowledgment

This work was supported by the National Science Foundation Grant No. 14-46765 and 14-27111. The authors would like to thank Bo Liu and the UIUC Intelligent Robotics Laboratory for help and support with the UGV used in this work.

References

[1] A. Jovicic, "Qualcomm Lumicast: A high accuracy indoor positioning system based on visible light communication," Qualcomm Whitepaper, April 2016.

[2] Y. Li, Z. He, J. Nielsen, and G. Lachapelle, "Using Wi-Fi/Magnetometers for Indoor Location and Personal Navigation," in *Int. Conf. on Indoor Positioning and Indoor Navigation (IPIN)*, Oct 2015, pp. 1–7.

[3] S. Wang, H. Wen, R. Clark, and N. Trigoni, "Keyframe based Large-Scale Indoor Localisation using Geomagnetic Field and Motion Pattern," in *IEEE/RSJ Int. Conf. on Intell. Robots and Syst. (IROS)*, Oct 2016, pp. 1910–1917.

[4] M. Frassl, M. Angermann, M. Lichtenstern, P. Robertson, B. J. Julian, and M. Doniec, "Magnetic Maps of Indoor Environments for Precise Localization of Legged and Non-legged Locomotion," in *IEEE/RSJ Int. Conf. on Intell. Robots and Syst. (IROS)*, Nov 2013, pp. 913–920.

[5] I. Vallivaara, J. Haverinen, A. Kemppainen, and J. Röning, "Magnetic field-based SLAM method for solving the localization problem in mobile robot floor-cleaning task," in *Int. Conf. on Advanced Robotics (ICAR)*, June 2011, pp. 198–203.

[6] (2017, May) MPU-6500. InvenSense. [Online]. Available: https://tinyurl.com/lhvrohm

[7] (2017, May) NXP/Freescale MAG3110GCR1. Mouser Electronics. [Online]. Available: https://tinyurl.com/mcff4z9

[8] J. Morrissey, "Request for proposal mvBlueFOX-MLC," email, Digital Network Vision, LLC, May 2015.

[9] (2017, May) PUCK VLP-16. Velodyne LiDAR. [Online]. Available: http://velodynelidar.com/vlp-16.html

[10] (2017) IndoorAtlas. [Online]. Available: www.indooratlas.com

[11] S. Shahidi and S. Valaee, "GIPSy: Geomagnetic Indoor Positioning System for Smartphones," in *Int. Conf. on Indoor Positioning and Indoor Navigation (IPIN)*, Oct 2015, pp. 1–7.

[12] J. Torres-Sospedra, D. Rambla, R. Montoliu, O. Belmonte, and J. Huerta, "UJIIndoorLoc-Mag: A New Database for Magnetic Field-Based Localization Problems," in *Int. Conf. on Indoor Positioning and Indoor Navigation (IPIN)*, Oct 2015, pp. 1–10.

[13] S.-E. Kim, Y. Kim, J. Yoon, and E. S. Kim, "Indoor Positioning System Using Geomagnetic Anomalies for Smartphones," in *Int. Conf. on Indoor Positioning and Indoor Navigation (IPIN)*, Nov 2012, pp. 1–5.

[14] C. Huang, S. He, Z. Jiang, C. Li, Y. Wang, and X. Wang, "Indoor Positioning System Based on Improved PDR and Magnetic Calibration Using Smartphone," in *Int. Symposium on Personal, Indoor, and Mobile Radio Communication (PIMRC)*, Sept 2014, pp. 2099–2103.

[15] J. Singh, K. Mori, S. Sidhu, and F. Mokaya, "Indoor Hallway Structure Mapping By Matching Segments From Crowd-sourced Mobile Traces," in *Int. Conf. on Indoor Positioning and Indoor Navigation (IPIN)*, Oct 2015, pp. 1–10.

[16] C. Gao and R. Harle, "Sequence-based Magnetic Loop Closures for Automated Signal Surveying," in *Int. Conf. on Indoor Positioning and Indoor Navigation (IPIN)*, Oct 2015, pp. 1–12.

[17] P. Mirowski, T. K. Ho, S. Yi, and M. MacDonald, "SignalSLAM: Simultaneous Localization and Mapping with Mixed WiFi, Bluetooth, LTE and Magnetic Signals," in *Int. Conf. on Indoor Positioning and Indoor Navigation (IPIN)*, Oct 2013, pp. 1–10.

[18] R. Faragher and R. Harle, "Towards an Efficient, Intelligent, Opportunistic Smartphone Indoor Positioning System," *Navigation*, vol. 62, no. 1, pp. 55–72, 2015.

[19] R. Hostettler, W. Birk, and M. L. Nordenvaad, "Joint Vehicle Trajectory and Model Parameter Estimation using Road Side Sensors," *IEEE Sensors J.*, vol. 15, no. 9, pp. 5075–5086, Sept 2015.

[20] J. Jung, S. M. Lee, and H. Myung, "Indoor Mobile Robot Localization and Mapping Based on Ambient Magnetic Fields and Aiding Radio Sources," *IEEE Trans. Instrum. Meas.*, vol. 64, no. 7, pp. 1922–1934, July 2015.

[21] N. Akai and K. Ozaki, "Gaussian Processes for Magnetic Map-Based Localization in Large-Scale Indoor Environments," in *IEEE/RSJ Int. Conf. on Intell. Robots and Syst. (IROS)*, Sept 2015, pp. 4459–4464.

[22] P. Barsocchi, A. Crivello, D. L. Rosa, and F. Palumbo, "A multisource and multivariate dataset for indoor localization methods based on WLAN and geo-magnetic field fingerprinting," in *Int. Conf. on Indoor Positioning and Indoor Navigation (IPIN)*, Oct 2016, pp. 1–8.

[23] S. Sarkka, V. Tolvanen, J. Kannala, and E. Rahtu, "Adaptive Kalman Filtering and Smoothing for Gravitation Tracking in Mobile Systems," in *Int. Conf. on Indoor Positioning and Indoor Navigation (IPIN)*, Oct 2015, pp. 1–7.

[24] N. El-Sheimy, H. Hou, and X. Niu, "Analysis and Modeling of Inertial Sensors Using Allan Variance," *IEEE Trans. Instrum. Meas.*, vol. 57, no. 1, pp. 140–149, January 2008.

[25] J. Sturm, N. Engelhard, F. Endres, W. Burgard, and D. Cremers, "A Benchmark for the Evaluation of RGB-D SLAM Systems," in *IEEE/RSJ Int. Conf. on Intell. Robots and Syst. (IROS)*, Oct 2012, pp. 573–580.

[26] E. Olson, "AprilTag: A robust and flexible visual fiducial system," in *IEEE Int. Conf. on Rob. and Autom. (ICRA)*, May 2011, pp. 3400–3407.

[27] V. Renaudin, M. H. Afzal, and G. Lachapelle, "Complete Triaxis Magnetometer Calibration in the Magnetic Domain," *Journal of Sensors*, 2010.

[28] P. G. Savage, *Strapdown Analytics: Part 1*, 2nd ed. Maple Plain, MN: Strapdown Associates, Inc., 2007.

[29] C. E. Rasmussen and H. Nickisch, "Gaussian Processes for Machine Learning (GPML) Toolbox," *Journal of Machine Learning Research*, vol. 11, pp. 3011–3015, Nov 2010.

[30] M. Bauer, M. van der Wilk, and C. E. Rasmussen, "Understanding Probabilistic Sparse Gaussian Process Approximations," in *Advances in Neural Information Processing Systems 29*, D. D. Lee, M. Sugiyama, U. V. Luxburg, I. Guyon, and R. Garnett, Eds. Curran Associates, Inc., 2016, pp. 1533–1541.

[31] D. Hanley and T. Bretl, "An Improved Model-Based Observer for Inertial Navigation for Quadrotors with Low Cost IMUs," in *AIAA Guidance, Navigation, and Control Conf., AIAA SciTech Forum*, San Diego, CA, Jan. 2016.

[32] P. Robertson, M. Frassl, M. Angermann, M. Doniec, B. J. Julian, M. G. Puyol, M. Khider, M. Lichtenstern, and L. Bruno, "Simultaneous Localization and Mapping for Pedestrians using Distortions of the Local Magnetic Field Intensity in Large Indoor Environments," in *Int. Conf. on Indoor Positioning and Indoor Navigation (IPIN)*, Oct. 2013, pp. 1–10.

(a) Computer Cart

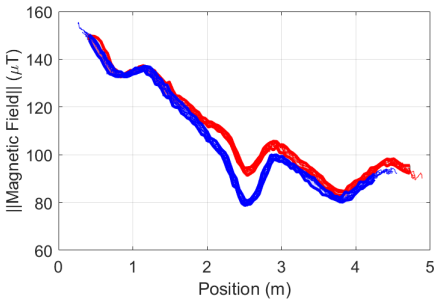

(b) Magnitude of magnetic field near computer cart.

(c) Bicycle

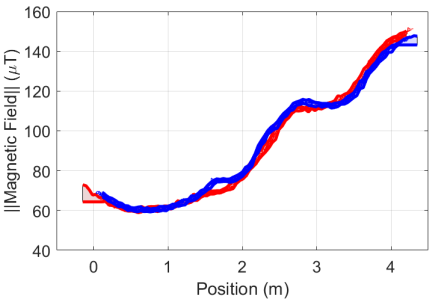

(d) Magnitude of magnetic field near bicycle.

(e) Computers Turned On

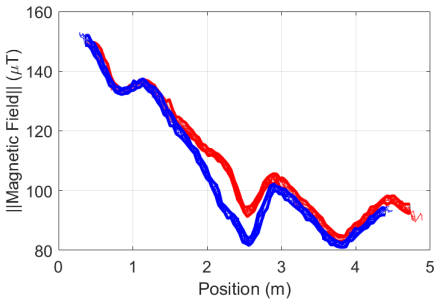

(f) Magnitude of magnetic field near computer which are turned on.

(g) Industrial Fan

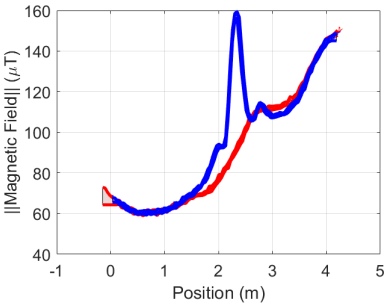

(h) Magnitude of magnetic field near fan.

(i) Cart with Refrigerator and Microwave

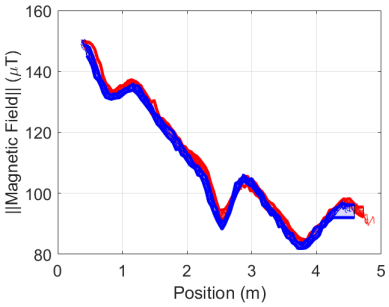

(j) Magnitude of magnetic field near cart with kitchen items.

(k) Metal Trash Can.

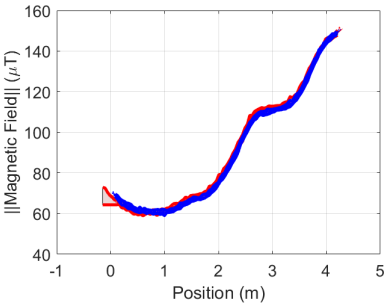

(l) Magnitude of magnetic field near metal trash can.

(m) Table and Chairs

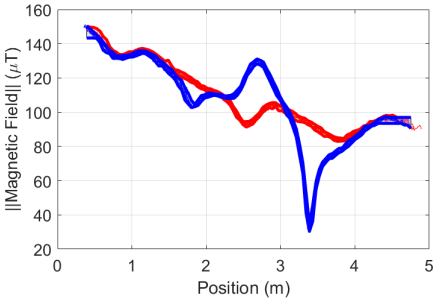

(n) Magnitude of magnetic field near table and chairs.

(o) Toolbox

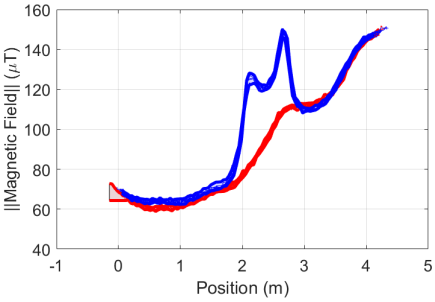

(p) Magnitude of magnetic field near toolbox.

Fig. 10. We consider a UGV proceeding down a hallway 20 times. Ten times without a potential "live magnetic load" present (red tube of sample paths) and ten times with a set of potential "live magnetic loads" in the hallway (blue tube of sample paths). The pictures and plots above display these selected candidate live magnetic loads and the corresponding norm of the magnetic field as a function of the distance down the hallway for the 20 trials. Several of these candidates clearly alter the magnetic field in the hallway.